Journal of Engineering and Technology for Industrial Applications

ISSN ONLINE: 2447-0228

ITEGAM-JETIA

Manaus, v.12 n.58, p.1188-1204. March/April, 2026.
DOI: https://doi.org/10.5935/jetia.v12i58.3288

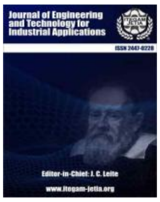

RESEARCH ARTICLE OPEN ACCESS

# DESIGN AND OPTIMIZATION OF MICRO-BLADE PASSIVE FLOW CONTROL FOR TOTAL PRESSURE LOSS REDUCTION IN AN AXIAL COMPRESSOR CASCADE

**Oussama Hachelfi*[1], Riyadh Belamadi[2], Naouam Boudinar[3]**

[1, 2, 3]National Higher School of Technology and Engineering, Laboratory of Energy Systems Technologies (LTSE), 23005 Annaba, Algeria.

[1]http://orcid.org/0009-0001-5062-1193, [2]http://orcid.org/0000-0003-1623-3602, [3]http://orcid.org/0000-0002-7291-0172

Email: *o.hachelfi@etu.ensti-annaba.dz, r.belamadi@ensti-annaba.dz, n.boudinar@ensti-annaba.dz

**ARTICLE INFO**

**Article History**
Received: January 11, 2026
Reviewed: February 13, 2026
Accepted: March 25, 2026
Published: April 30, 2026

**Keywords:**
Passive flow control,
Micro-blade,
Stall,
Boundary layer,
Corner separation.

## ABSTRACT

The present paper investigates the aerodynamic influence of a micro-blade (MB) flow control in a low-speed axial compressor cascade, through a combined two-dimensional (2D) optimization and three-dimensional (3D) validation framework. The influence of the MB's key geometric parameters, including chord length, camber angle, stagger angle, and maximum thickness, as well as spatial positioning, was systematically analyzed to identify the optimal configuration. Results reveal a size-wake trade-off; small elements fail to sustain meaningful momentum exchange, whereas large elements introduce excessive blockage and wake losses. An intermediate chord of 20% of the main blade, combined with a medium element maximum thickness (5% of the MB chord) and 50° camber, provides the most favorable compromise, achieving a 55.56% reduction in total pressure loss coefficient (TPL) under stall conditions. The optimized MB was subsequently evaluated in a 3D cascade configuration to examine its influence on corner separation and 3D flow structures across design and off-design inlet flow angles. The 3D results showed a clear reduction in the corner separation spanwise extent, especially at high incidences, though a TPL penalty is observed at the nominal design angle, where the baseline flow is already attached. Overall, the findings demonstrate that carefully optimized MB can effectively mitigate losses and enhance compressor operability when geometry and placement are properly designed.

## I. INTRODUCTION

Modern axial compressors are increasingly facing performance demands over a wide range of operating conditions. The pursuit of a higher-pressure ratio and lower fuel consumption has involved a higher blade loading, and consequently, the emergence of complex flow phenomena such as boundary layer separation, corner stall, and secondary flows is now inevitable. In low-speed compressors, such flow phenomena produce low-momentum zones that can block the flow and reduce static pressure rise, leading to increasing losses and risking stall [1]. Passive flow control techniques have emerged as effective solutions to mitigate these adverse flow phenomena with simplicity and without any external energy input, unlike active control systems [2]. These devices use small geometric modifications to energize the boundary layer or redistribute the secondary flow. For example, vortex generators and endwall fences have been shown to create streamwise vortices that suppress crossflow and corner stall, thereby extending the stall margin [3-7]. Such passive devices have contributed to notable gains; the addition of a vortex generator (VG) to a highly loaded compressor cascade reduced the total pressure losses by about 8.3% [8], and a strategically placed endwall fence was reported to reduce the loss coefficient up to 9% [9]. These results highlight that surface additions (or cuts) can significantly improve compressor performance. Beyond conventional VGs and slots, micro-scale flow control elements are currently attracting interest. For example, micro-vortex generators (MVGs) of various shapes can delay stall and reduce losses by about 9.36% [10].

More recently, a “fish scale” array applied to the suction side has been experimentally shown to generate small upward vortices that entrain the low-momentum endwall flow; this design reduces the total pressure loss by 5.69% [11]. Such studies demonstrate that even very small passive elements can improve mixing and reduce separation in low-speed compressor flows. In parallel with these advances, a promising approach has received little focus; discrete micro-blades (small airfoil) placed in the passage upstream of the separation onset. Unlike shallow ribs or ramps, a full-span micro-blade could generate a “suction surface jet” [12], preventing the buildup of low-momentum fluid in the passage region. Ma & Sun [13] investigated the spatial positioning of a “little blade,” focusing on its placement within the cascade passage. Their work demonstrated a measurable sensitivity to axial positioning according to incidence angle; similarly, Guo et al. [14] explored the impact of different spatial locations, stagger angles, and heights of a “little blade”, with the optimal configuration yielding a 10.38% drop in the total pressure loss coefficient at near-stall condition.

However, optimizing these devices for practical applications remains difficult due to the complex interactions between the device geometry, spatial positioning, and operating conditions. The aerodynamic influence of the micro-blade’s geometric design parameters has received considerably less attention; most previous studies on micro-blades have mainly concentrated on the effects of spatial positioning, while the geometric optimization of the micro-blade itself remains largely unexplored. Building on this background, the present study conducts a comprehensive two-dimensional computational optimization of the combined effects of the micro-blade’s spatial positioning (axial and circumferential), geometric parameter design (stagger angle, camber angle, maximum thickness, chord length), and operating conditions (inflow angle) within a unified parametric framework, followed by a 3D investigation of the optimal configuration to verify its impacts on the corner separation and secondary flow. This comprehensive approach allows for the identification of parameter interactions and optimal configurations that would be missed by single-variable studies.

## II. METHOD

The numerical study was conducted on a low-speed linear compressor cascade employing the NACA 65(10)18 airfoil profile, using a chord length of c=0.127 m. The detailed geometrical specifications of the cascade are summarized in Table 1. Initially, a 2D investigation was carried out in order to conduct a systematic parametric study on the flow control element. The approach consists of successively modifying the geometric design parameters of a microblade (MB) under different inlet flow angles (β) and monitoring its impact on the aerodynamic performance of the cascade. In its primary state, the MB appears as a symmetric plate with a double-circular-arc (DCA) profile type and zero camber angle, positioned in the proximity of the main blade suction side (see Figure 7). An optimization process was then performed based on the MB’s spatial locations (axial and circumferential positions) and geometric design parameters, including camber angle, stagger angle, chord length, and maximum thickness at different off-design inlet flow angles.

Table 1: Geometric parameters of the compressor blade.

| Parameter | Value |
|---|---|
| Chord (m) | 0.127 |
| Solidity | 1.25 |
| Stagger angle (°) | 13 |
| Aspect ratio | 1 |

Source: Authors, (2026).

Once the optimal design and positions were identified in the 2D computational cases, the study was extended to a three–dimensional (3D) configuration. The 3D simulations served for the assessment of the influence of the MB on corner stall and flow structures.

### II.1 PERFORMANCE PARAMETERS

The aerodynamic performance of the compressor cascade was evaluated using global loss coefficients, and local boundary layer integral parameters. The total pressure loss coefficient (TPL) was employed as the primary metric to quantify aerodynamic losses, defined as

$$TPL = \frac{P_{t,1} - P_{t,2}}{P_{t,1} - P_1} \tag{1}$$

Where $P_{t,1}$ and $P_{t,2}$ denote the mass-averaged total pressure at the inlet and outlet boundary, respectively, and $P_1$ is the inlet static pressure. To evaluate the improvement (or deterioration), the change in TPL was introduced as:

$$\Delta TPL = TPL_{baseline} - TPL_{micro-blade} \tag{2}$$

Where positive values of $\Delta TPL$ indicate reduced losses, while negative values denote deterioration. The static pressure coefficient is defined as:

$$Cp = \frac{P - P_1}{P_{t,1} - P_1} \tag{3}$$

Here, P denotes the local static pressure. The mass-averaged Cp at the outlet boundary (Cp’) is employed to quantify the diffusion of the cascade [12]. To investigate boundary layer behavior, the classical integral parameters were extracted along the suction surface of the main blade. The displacement thickness $\delta^*$ and momentum thickness $\theta$ are given by:

$$\delta^* = \int_0^\infty \left(1 - \frac{u}{u_\infty}\right) dy \tag{4}$$

$$\theta = \int_0^\infty \frac{u}{u_\infty}\left(1 - \frac{u}{u_\infty}\right) dy \tag{5}$$

Where $u$ and $u_\infty$ are the local and free-stream velocities, respectively. The shape factor is given by:

$$H = \frac{\delta^*}{\theta} \tag{6}$$

The axial position (X) of the MB is expressed in percentage of the main blade axial chord, given by:

$$\mathrm{X} = \frac{d_x}{\mathrm{Cx}} \times 100 \tag{7}$$

Where $d_x$ represents the axial distance between the leading edges of the main and micro blades, and Cx is the main axial chord length. The circumferential position (Y) of the MB is expressed in percentage of pitch; it is given by:

$$\mathrm{Y} = \frac{d_y}{s} \times 100 \tag{8}$$

Where $d_y$ represents the circumferential distance measured from the leading edge of the MB to the main blade suction side, and s denotes the blade spacing length

## II.2 SOLVER SETTINGS AND NUMERICAL VALIDATION

A single-blade passage of NACA 65(18)10 linear compressor cascade was conducted using the commercial CFD solver Ansys Fluent, limited by periodic boundaries to represent the circumferential domain. The simulation employed the steady incompressible Reynolds-averaged Navier–Stokes (RANS) equations, closed using the two-equation k-ω shear stress transport (SST) as a turbulence model [15], chosen for its robustness in predicting adverse pressure gradient and boundary layer separations. The inlet boundary conditions were defined by specifying the free-stream velocity components, along with the corresponding turbulence intensity and characteristic length scale. The simulation was conducted under operating conditions corresponding to a chord-based Reynolds number of 245000. Constant thermophysical properties of air were assumed. Convergence was considered based on normalized residuals falling below $10^{-5}$ for continuity, momentum, and turbulence transport equations, with monitoring of TPL, and Cp on the blade surfaces.

### *III.2.1 Two-dimensional Cascade*

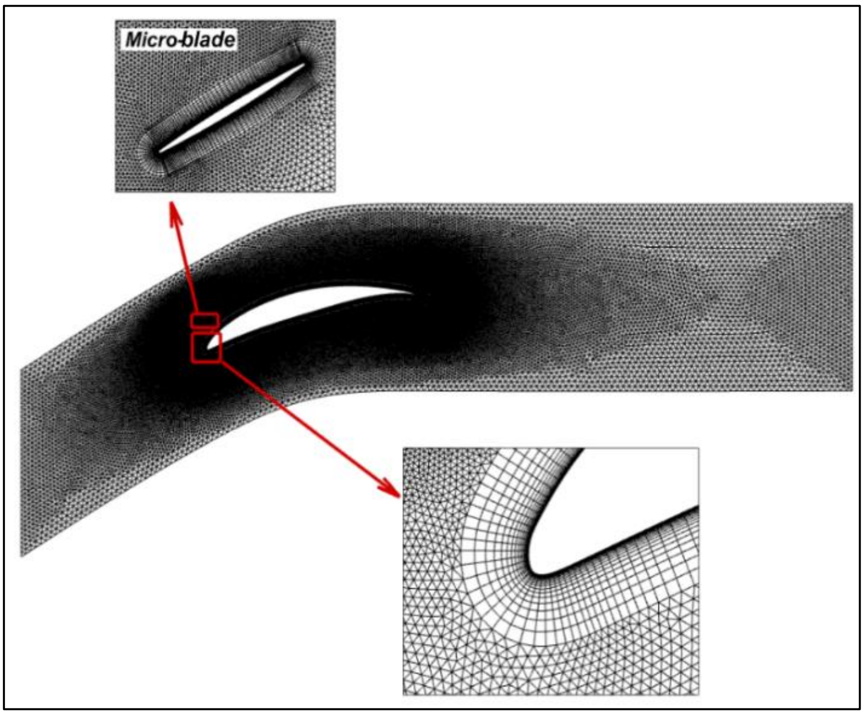

Figure 1: 2D Computational grid.
Source: Authors, (2026).

The 2D domain was meshed with a hybrid unstructured grid using Gambit software. Figure 1 shows the 2D computational grid of the controlled case. To precisely capture the boundary layer development, a refined clustering with 20 inflation layers was applied to all solid walls with 1.25 and 1.15 growth ratios for the main blade and the MB, respectively.

In order to guarantee $y+ < 1$, the first cell height at the walls was set to $1 \times 10^{-5}$ m, Figure 2 (right) shows the dimensionless first cell height at the blade wall boundary. A grid independence study was carried out by refining the mesh at boundaries and solid walls, as illustrated in Figure 2 (left). A final mesh size of about 76000 cells was selected, as further refinement produces negligible variation in TPL, with a total of 410 discretization points around the main blade airfoil.

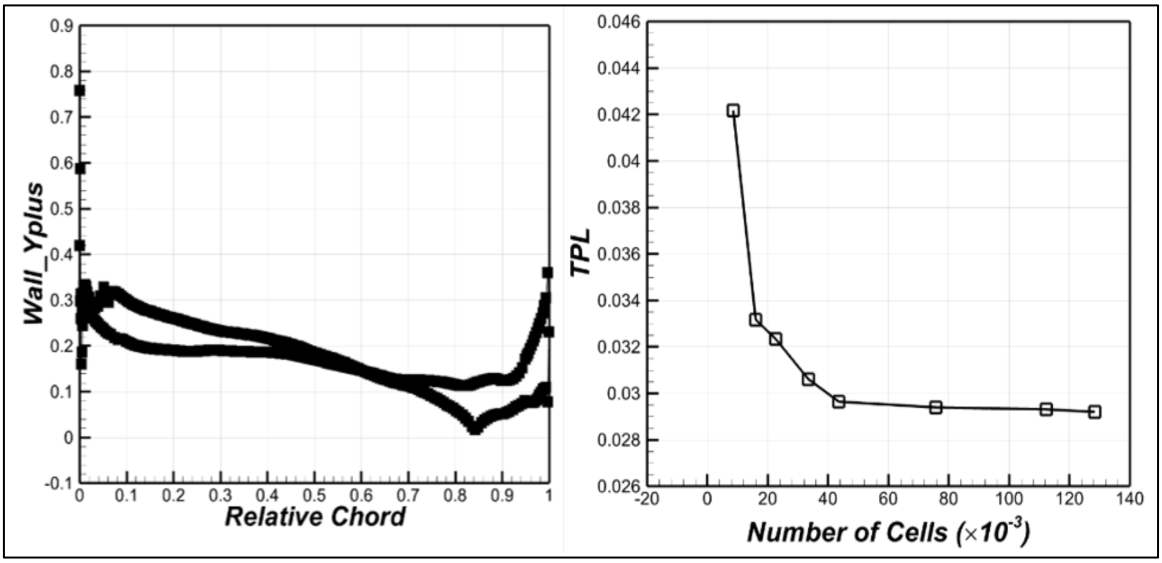

Figure 2: Dimensionless first cell height at the main blade walls (right), grid independence study (left).
Source: Authors, (2026).

To guarantee the reliability of the numerical setup, the calculated results of the baseline case (without flow control) were validated against the experimental measurements reported in [16]. Figure 3 shows the corresponding validation in terms of Relative Dynamic $S = 2(p_{t,1} - p)/(\rho {W_1}^2)$ (where $W_1$ is the upstream velocity), across the Relative Chord (x/c). The numerical results obtained using the k-ω SST turbulence model show excellent agreement with the experimental data.

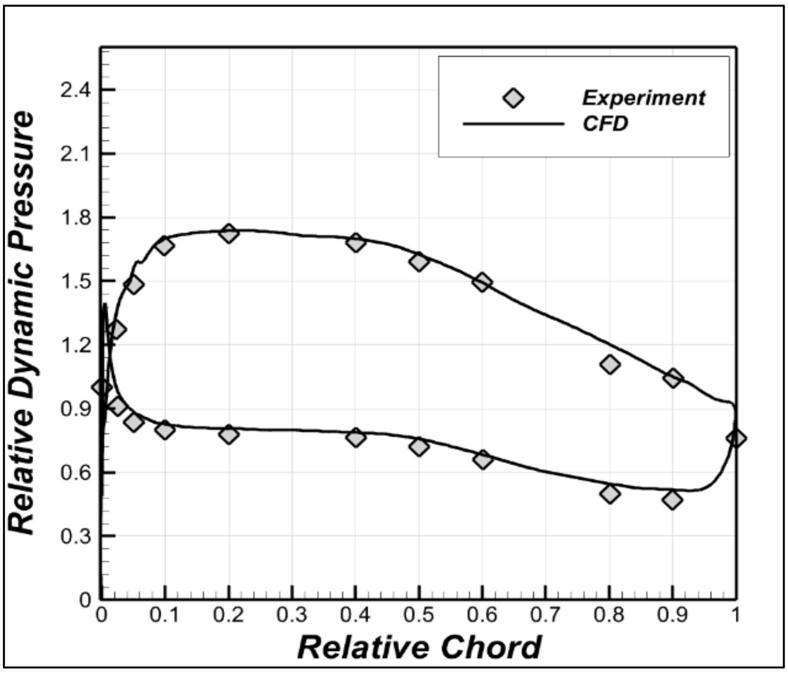

Figure 3: Comparison of measured and calculated relative dynamic pressure for the baseline configuration.
Source: Authors, (2026).

### II.2.2 Three-dimensional Cascade

Following the two-dimensional parametric study, the optimal MB configuration was further investigated in a three-dimensional cascade case to capture its effect on corner separation and 3D flow structures. The same airfoil geometry used in the 2D study was retained with the addition of an aspect ratio of AR=1 to maintain a representative three-dimensional configuration.

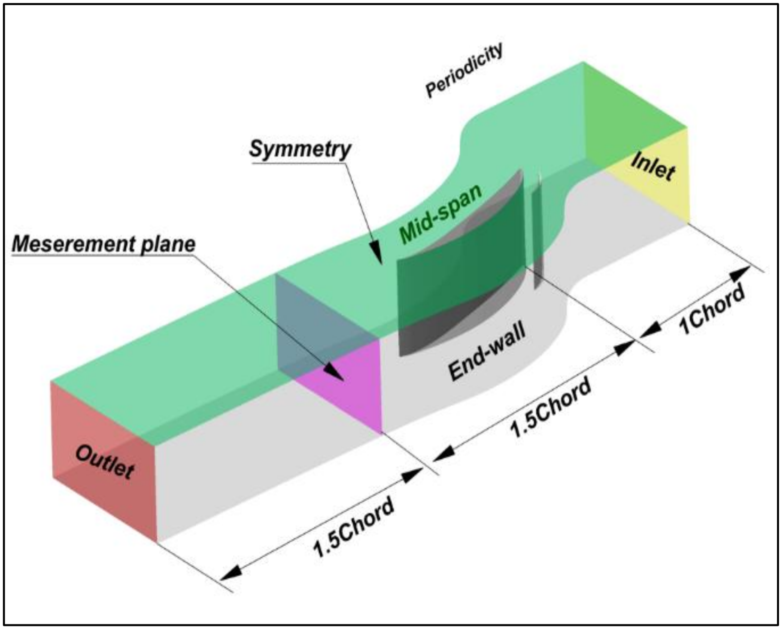

Figure 4: Computational 3D domain and boundary conditions.
Source: Authors, (2026).

Figure 4 illustrates the corresponding computational 3D domain and boundary conditions. By exploiting the symmetry of the geometry and to reduce computational costs, only half of the spanwise domain was modeled with a symmetry boundary condition imposed at the mid-span plane. The performance parameters were evaluated at a downstream location corresponding to 1.5 times the blade chord from the leading edge. Like the 2D computational case, the domain extends one chord length upstream of the leading edge and two chords downstream. The 3D computational grid was generated using Numeca Autogrid 5, employing a fully structured O4H topology (see Figure 5) to ensure high grid quality and low numerical diffusion. Special attention was given to the near wall region, with a first cell height of $1 \times 10^{-5}$ m, resulting in an average dimensionless wall distance $y+ < 1$ across all solid boundaries. A similar compressor cascade was modeled by Ramzi & AbdErrahmane [17], with full-span configuration using approximately 1 million grid points. However, in the present investigation, since only half of the span was considered, a mesh of about 855.000 points was adopted.

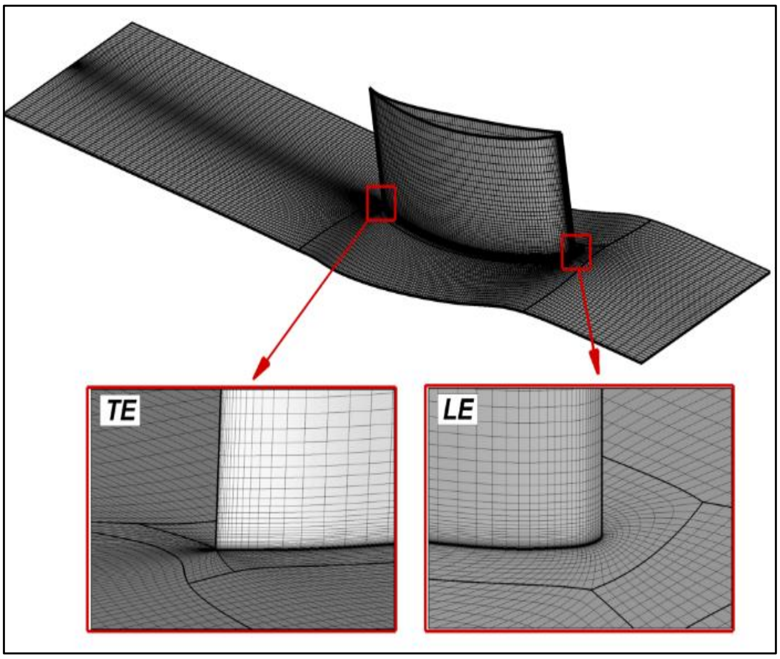

Figure 5: 3D Computational grid.
Source: Authors, (2026).

Direct numerical data of the NACA 65(18)10 cascade with endwall effects are not available, as the original tests were conducted under 2D conditions with endwall boundary layer removal [16]. In order to investigate the effectiveness of the optimal MB flow control on the 3D corner separation, it was necessary to adopt an alternative validation approach. Following the approach adopted by Ref. [17], the present solver was validated through comparison with the experimental data of Takahashi et al. [18], who investigated the 3D flow characteristics of a NACA 65 cascade. The reference cascade was characterized by an aspect ratio of AR=2.3, a solidity of 1.08, with 30.1° and 32.2°, camber and stagger angles, respectively. The experiments were performed at an inlet flow angle of 47.1° and a Reynolds number of $2.2 \times 10^5$ based on chord length.

The validation of the numerical model was carried out by comparing the circumferentially mass-averaged TPL across half of the blade span, at a downstream position of 1.5c from the leading edge, with the available experimental measurements. As shown in Figure 6, the numerical prediction follows the experimental trend, with only minor deviations, especially in the corner region. In general, the comparison shows good agreement, demonstrating the accuracy of the numerical setup in capturing endwall boundary layer development and corner separation. Consequently, although the geometry differs from the present cascade, the underlying physical mechanisms were validated. This provides confidence in applying the same numerical methodology to the current 3D configuration (NACA 65(18)10) with micro-blade flow control.

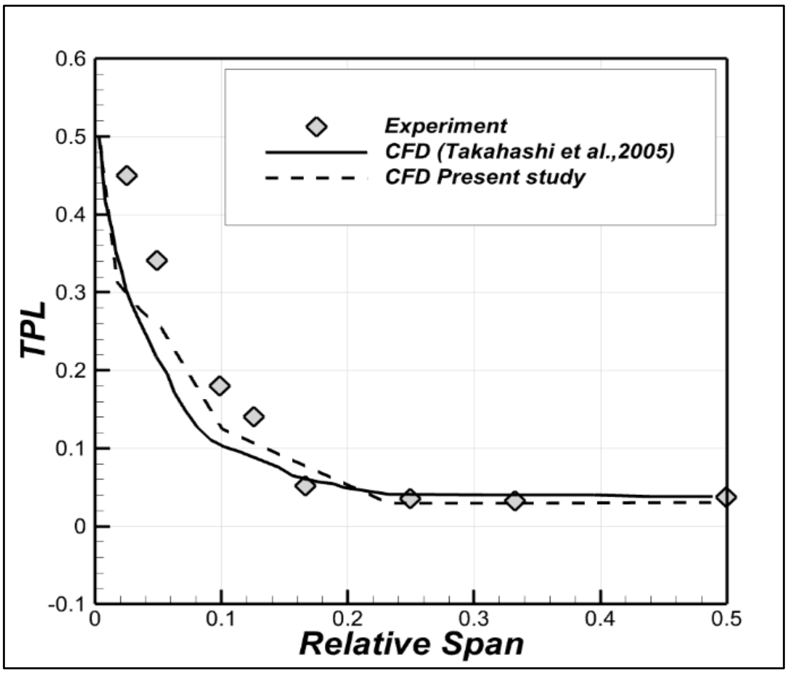

Figure 6: Comparison of experimental and numerical spanwise distribution of TPL across the half-span.
Source: Authors, (2026).

## III. RESULTS AND DISCUSSIONS

### III.1 SPATIAL LOCATION EFFECTS

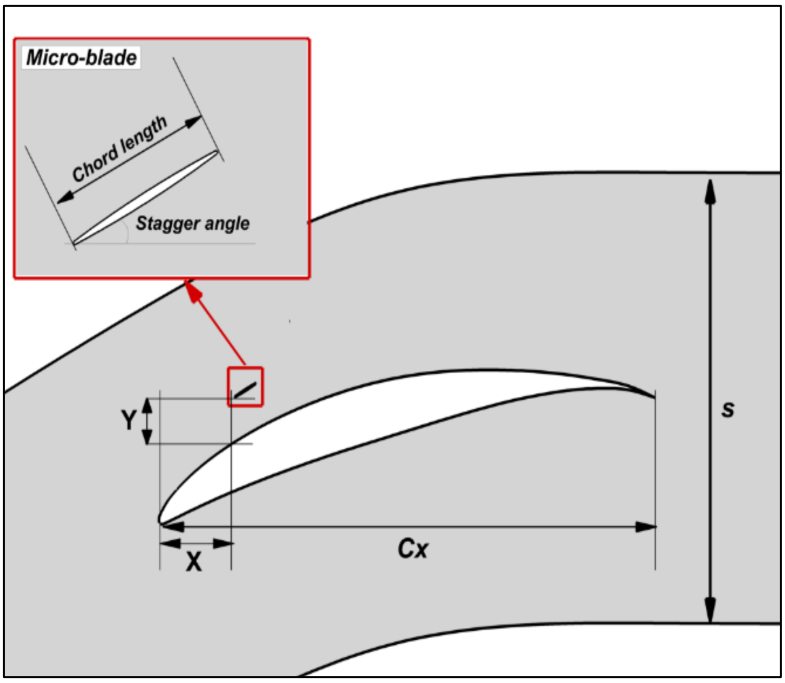

Figure 7: Micro-blade’s spatial positions nomenclature.
Source: Authors, (2026).

The first step in the present investigation is to determine the most effective spatial placement of the MB, as mentioned earlier, the initial MB is modeled as a DCA airfoil with zero camber angle; the chord length of the MB is expressed as a percentage of the main blade chord, ensuring a normalized representation. the primary design parameters of the flow control element are listed in Table 2.

Table 2: Initial design parameters of the micro-blade.

| Parameter | value |
|---|---|
| Chord (%) | 5 |
| $T_{max}/c_{MB}$ | 0.05 |
| Stagger angle (°) | 30 |
| Camber angle (°) | 0 |

Source: Authors, (2026).

The parametric study was performed by varying both axial and circumferential locations of the MB under different inlet flow angles, ranging from 40° to 52° with a 2° increment, generating 16 distinct configurations and a total of 112 simulations, ensuring that the influence of spatial locations was captured with sufficient resolution. Figure 8 illustrates all the tested locations; the axial position of the MB (X) was varied from -5% to 40%, while the circumferential (Y) placement corresponded to 10% and 15%. For each configuration, ΔTPL was evaluated.

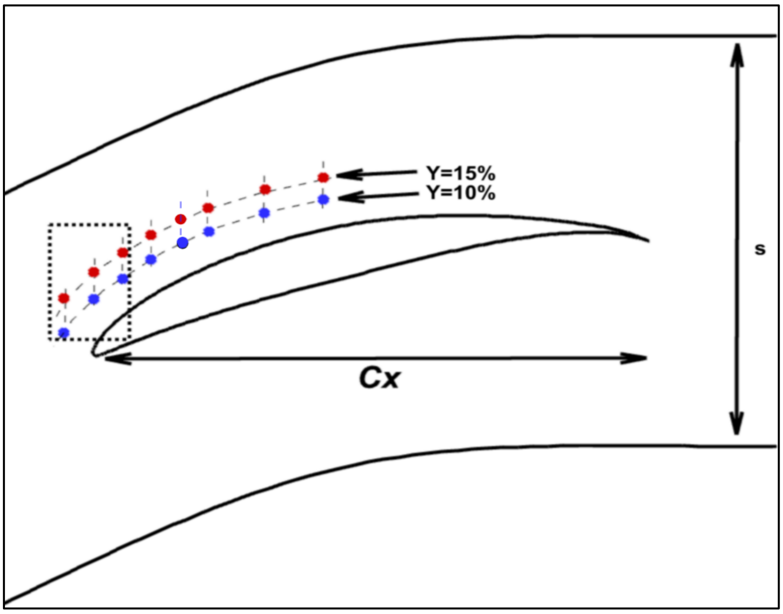

Figure 8: Schematic representation of axial and circumferential positions of the MB configurations.
Source: Authors, (2026).

Figure 9 presents the distribution of ΔTPL across the whole range of tested inlet flow angles. The Figure shows a high sensitivity to the device's axial placement compared with the circumferential locations. The maximum improvement of ΔTPL was achieved at 3 axial locations X=-5%, X=0% and X=+5%, it was also reported by Ma & Sun [13] that the optimal placement is consistently near the blade leading edge. The examination of Figure 9 allowed us to delineate an effective range of the MB axial locations (X= -5%, 0%, +5%). To provide a clearer comparison, the ΔTPL associated with these selected configurations were summarized in a bar chart in Figure 10.

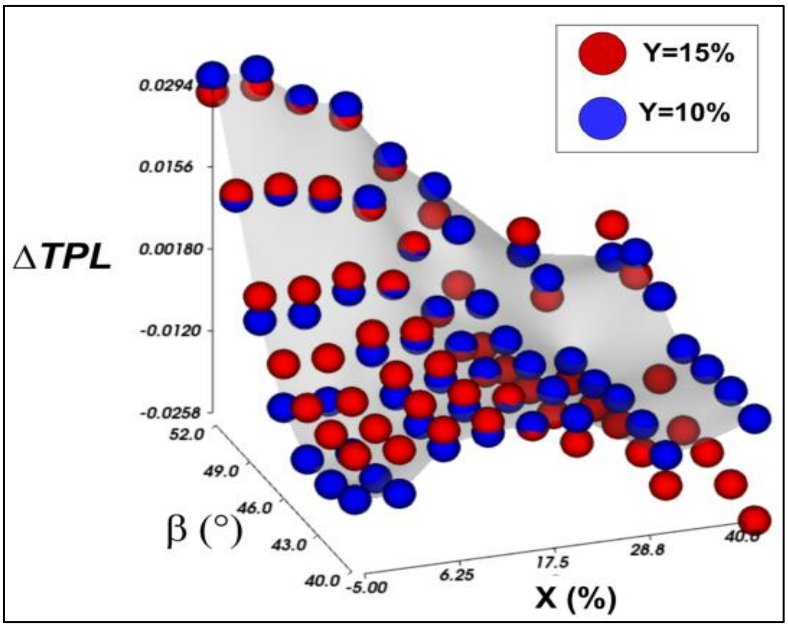

Figure 9: Point-cloud distribution of ΔTPL for Y=15% and Y=10%, versus axial MB's locations in different inlet flow angles.
Source: Authors, (2026).

At inlet flow angles (40° to 48°), the majority of the configurations increase the losses (ΔTPL<0), adding the MB at this range of incidence tends to generate additional losses, the baseline flow at those operating conditions is already separated, but though not yet in a severe way. the extra mixing induced by the MB disturbs the flow, hence, ends up raising the overall losses. At high inlet flow angles (50° to 52°), the flow over the baseline blade is strongly separated due to the severe adverse pressure gradient. Under these conditions, the MB becomes particularly effective, producing positive ΔTPL values and a net reduction in the global losses. However, the influence of the circumferential location is almost identical, with a slight superiority at Y=10%. Regarding axial placement, X=−5% demonstrated the largest improvements in ΔTPL, especially at high β, while its sensitivity to operating conditions suggests that additional checks are necessary. Based on these observations, the Y=10% circumferential position is retained for subsequent analyses.

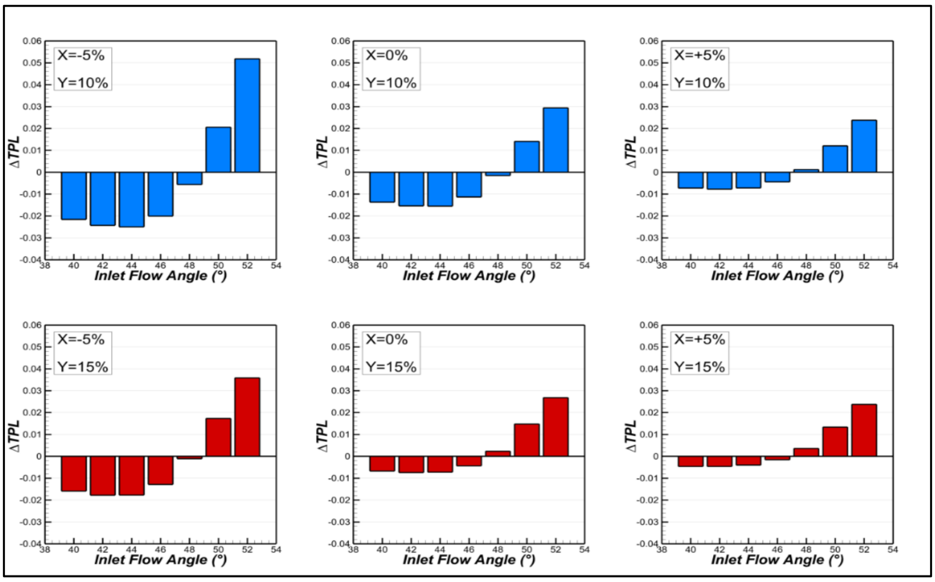

Figure 10: Bar chart of ΔTPL at Y=10% (up) and Y=15% (down) for the three axial position X=-5%, X=0% and X=+5%.
Source: Authors, (2026).

### III.2 CAMBER ANGLE EFFECTS

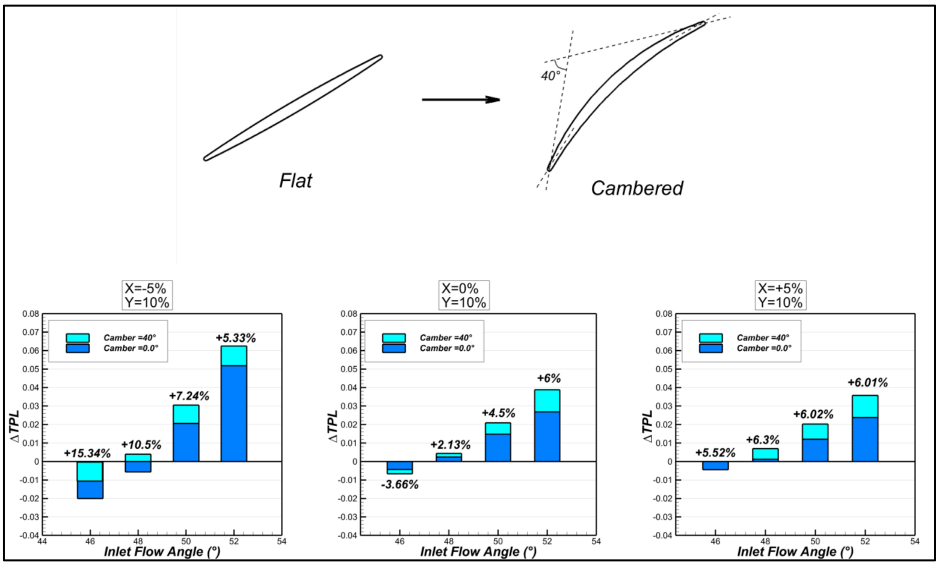

Figure 11: Bar chart of ΔTPL for flat and cambered MB at X=−5%, X=0% and X=+5% across different off-design β.
Source: Authors, (2026).

To further investigate the sensitivity of the device to its geometric characteristics, the effect of introducing a camber angle of 40° to the MB was examined. Figure 11 presents the corresponding sketch (up), and bar chart (down) of the ΔTPL for the three axial positions X=−5%, X=0%, and X=+5%, with and without camber, across off-design inlet flow angles (46° to 52° with 2° increment), the results indicate that the addition of a 40° camber angle consistently enhances the effectiveness of the MB, a remarkable improvement in the ΔTPL across the whole tested range, amplifying the benefit effect observed with zero camber MB. In addition to the TPL analysis, the effect of cambering the MB was further examined through the distribution of the static pressure coefficient (Cp) on the main blade suction side. Figure 12 (left) shows the corresponding Cp curves for the three tested locations at β=52°. The presence of camber introduces a local peak in the Cp, which originates mainly from the concave curvature of the MB pressure suroussmahachelfiface (see Figure 12, right), indicating a local deceleration in the immediate vicinity of the common passage sectional area between the main blade and the MB. On the other hand, the flat MB produces a local pressure decrease (depression) in the same region, unlike the cambered case, the flat MB produces a local acceleration on the main blade suction surface. This is mainly attributed to the convergent-divergent-like channel [19] between the flat MB and the suction side of the main blade.

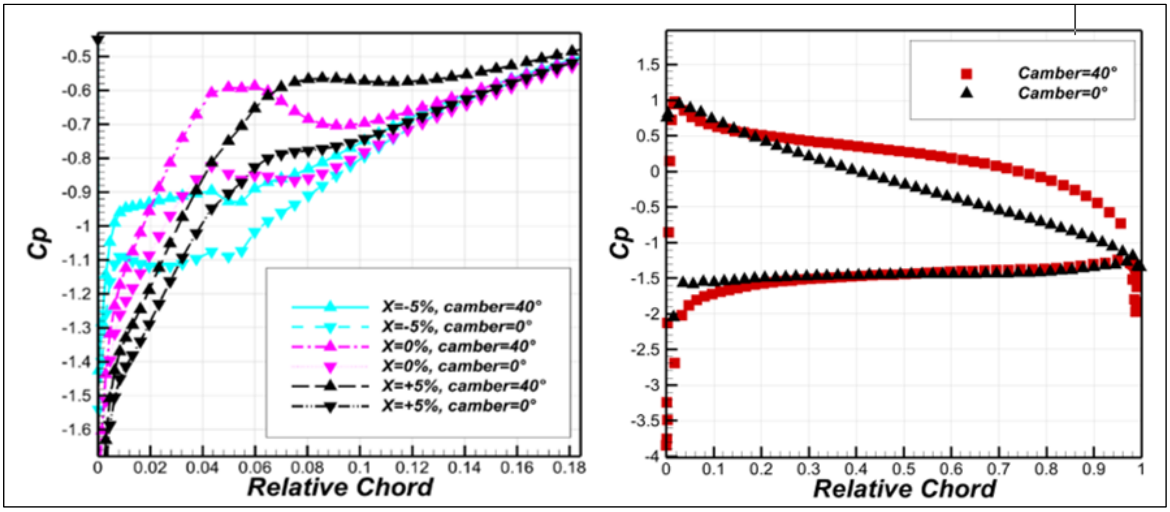

Figure 12: Static pressure coefficient of the main blade suction side (left) and MB (right) at β=52°.
Source: Authors, (2026).

The divergent local pressure features imply different local velocity fields and boundary layer behaviors. The corresponding boundary layer integral parameters were calculated using a MATLAB code. Figure 13 presents the chordwise evolution of the displacement thickness, momentum thickness, and shape factor for the baseline, flat, and cambered MB in two representative inlet flow angles of 46° and 52°.

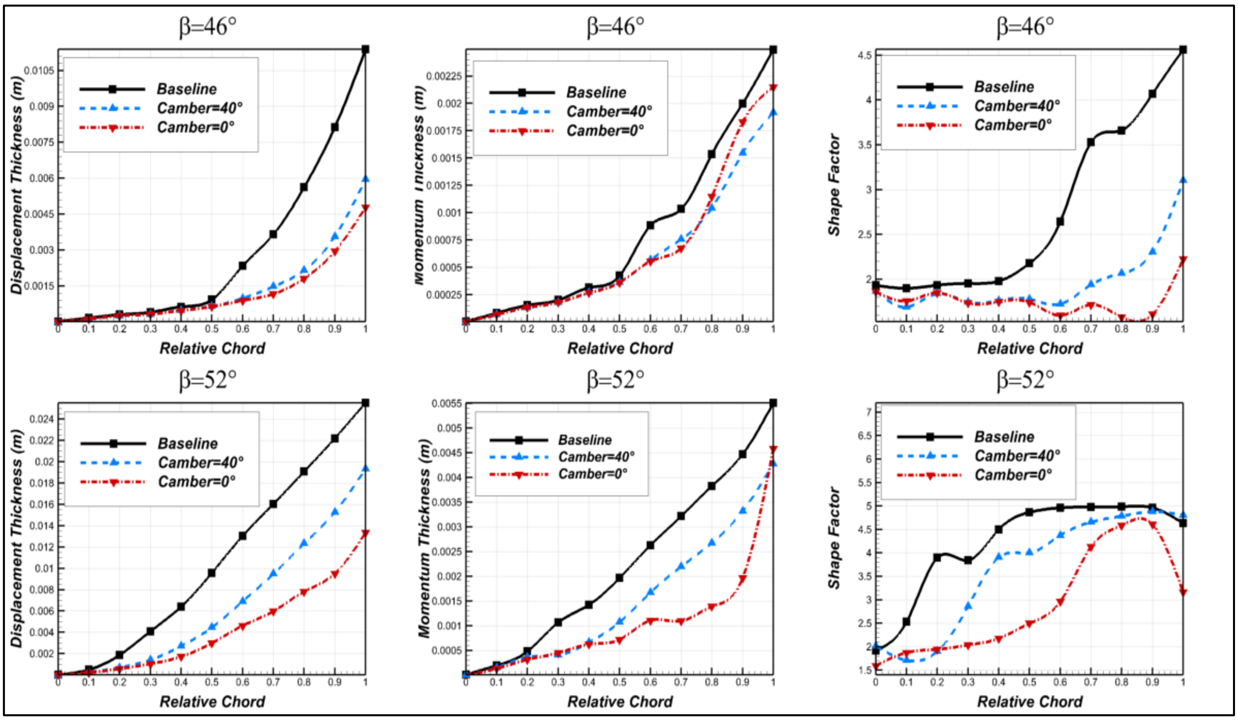

Figure 13: Displacement thickness, momentum thickness, and shape Factor distributions along the suction side main blade at 46° (up) and 52° (down) inlet flow angles for baseline, flat, and cambered MB configurations.
Source: Authors, (2026).

At 46° inlet flow angle, the baseline configuration exhibits the highest displacement and momentum thickness, and consequently a rapidly increasing shape factor at approximately the half-chord station toward the trailing edge. This behavior indicates the beginning of separation at nearly 50% of the chord length, extending to the leading edge. Both the flat and cambered configurations reduce displacement and momentum thicknesses over the entire suction surface, indicating a global boundary layer delay in separation relative to the baseline. This effect is particularly pronounced at 52°, while the baseline configuration experiences a severe boundary layer thickening, both MB cases maintain a much thinner boundary layer. When comparing the two MB designs, at both inlet flow angles, the cambered case shows higher momentum, displacement thickness, and shape factor, in most of the chord stations. The flat configuration demonstrates superior performance; its corresponding shape factor remains consistently lower over a large portion of the chord, indicating a much resistant boundary layer over the whole chord stations, and at different inlet flow angles. This is consistent with the depression reported in the Cp curve in Figure 12, highlighting the ability of the flat MB to entrain higher momentum freestream fluid and sustain a more energized boundary layer. This is further evidenced by the lower shape factor values, which reflect a delayed separation onset and improved boundary layer stability

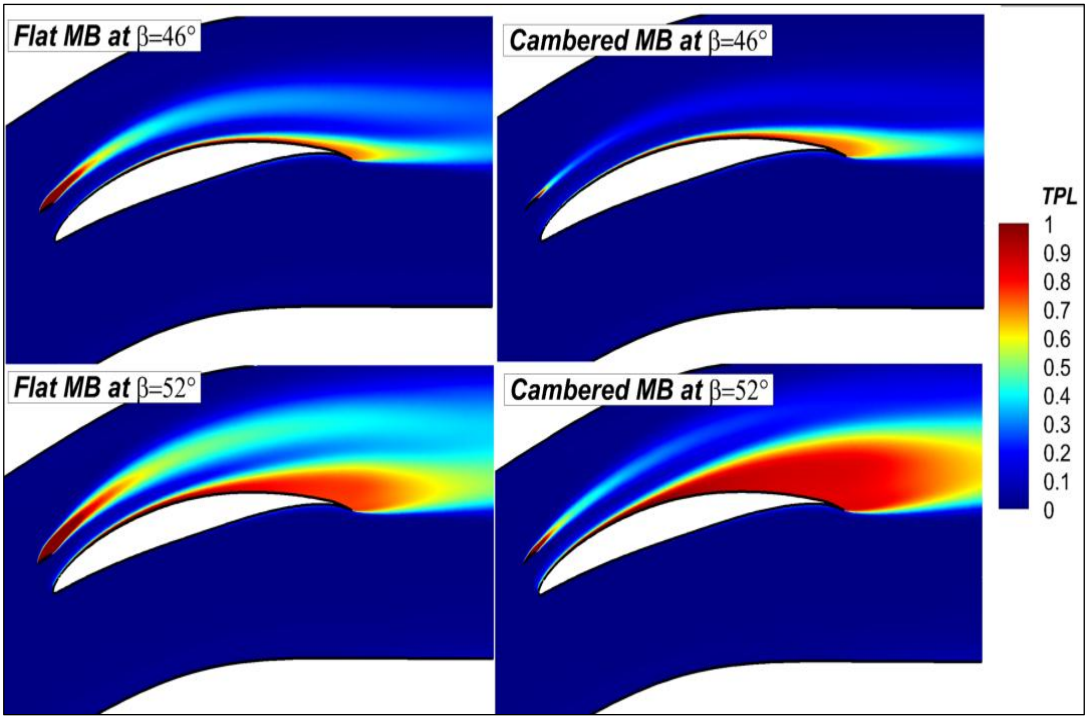

Figure 14: TPL contours for flat and cambered MB at 46° and 52° inlet flow angles.
Source: Authors, (2026).

In parallel, the flat MB, although generating a thinner boundary layer, shows a slightly higher momentum thickness than the cambered case at the trailing edge region, and promotes an early interaction between its wake and the separated boundary layer of the main blade near the trailing edge. This behavior is in agreement with the *TPL* contours shown in Figure 14, where the flat configuration exhibits an enlarged wake region that merges with the separated boundary layer of the main blade suction side, whereas the cambered case shows a more confined wake due to its aerodynamic shape (Figure 15). Hence, the superior global performance of the cambered MB comes not from its immediate effect on the boundary layer, but from its capacity to maintain both boundary layer stability and less wake losses. To further refine the optimal MB design, and building on this result, the next section examines the combined effect of camber angle and maximum thickness of the MB.

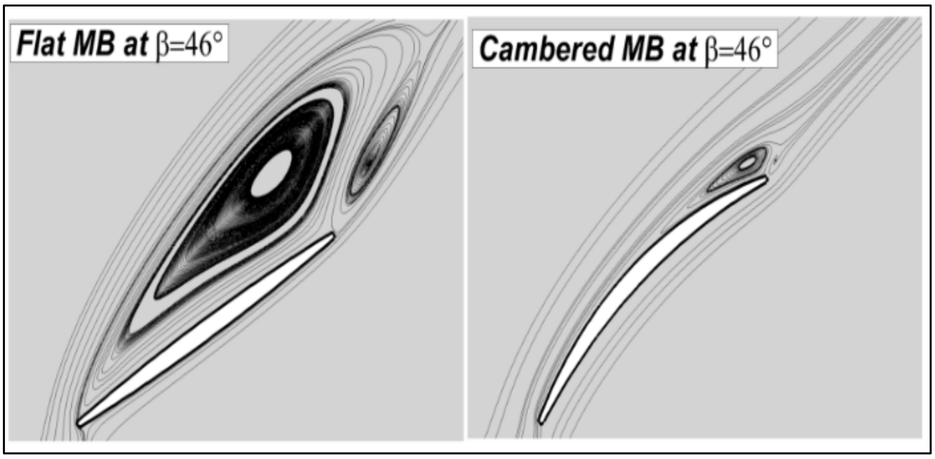

Figure 15: Velocity streamlines for Flat (left), and cambered (right) micro-blades.
Source: Authors, (2026).

### III.3 MAXIMUM THICKNESS AND CAMBER ANGLE COMBINATION EFFECTS

The influence of MB camber and maximum thickness on the cascade losses was evaluated for three element thicknesses: thin =2.5%□□□, medium =5%□□□, and thick =10%□□□ at four representative off-design inlet flow angles (□= 46°, 48°, 50°, 52°). As illustrated in Figure 16, thinner elements produce lower TPL while thicker elements give the largest losses. In parallel, increasing camber generally reduces TPL, with the effect becoming more pronounced at higher incidence (largest reductions at β =50°, 52°). At moderate incidence (46° to 48°), the TPL–camber curves show a shared minimum corresponding to 30° and 40° camber angles, except for the medium thickness MB reaches the lower minimum with 50° camber angle at β=48°, whereas at high incidence (50° to 52°) the curves decline more sharply and larger camber continues to be beneficial. Although the thin MB attains the best minima in most cases, it exhibits greater sensitivity to camber angle, especially at β=48°. While the medium thickness MB yields TPL values close to the thin case, the thick MB configuration is systematically inferior.

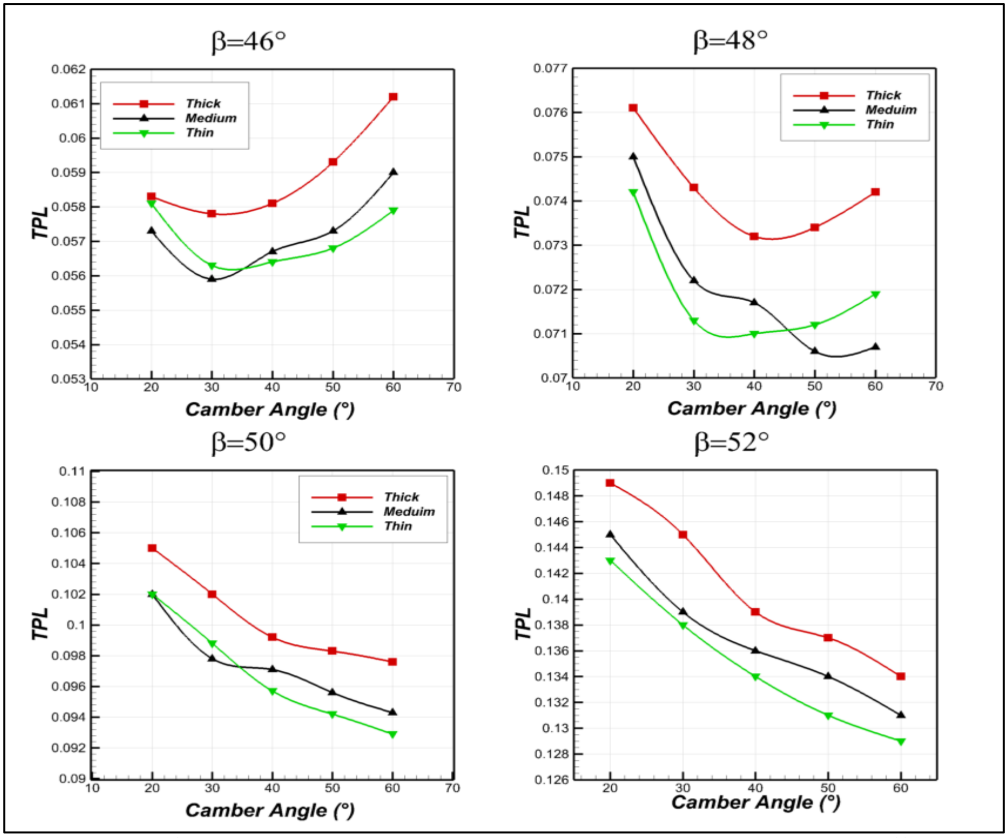

Figure 16**:** TPL versus camber Angle for Three Micro-Blade Thicknesses (thin, medium, and thick) at Different Inlet Flow Angles.
Source: Authors, (2026).

The results of the camber sweep highlighted two configurations of particular interest: the thin MB with 40° camber, which demonstrated the lowest TPL considering the whole tested β range, and the medium with 50° camber, which achieved comparable reductions in global losses while maintaining a more stable response over the tested incidences. Figure 17 shows the static pressure rise coefficient (Cp') for the two cases; the medium configuration provided a modest but clear advantage; the additional MB loading provided by the higher camber angle within the medium MB case has contributed to the improvement of the overall Cp'. Considering this complementary improvement in static pressure rise and both aerodynamic efficiency and practical considerations (mechanical resistance), the medium configuration with 50° camber angle was selected for further optimizations.

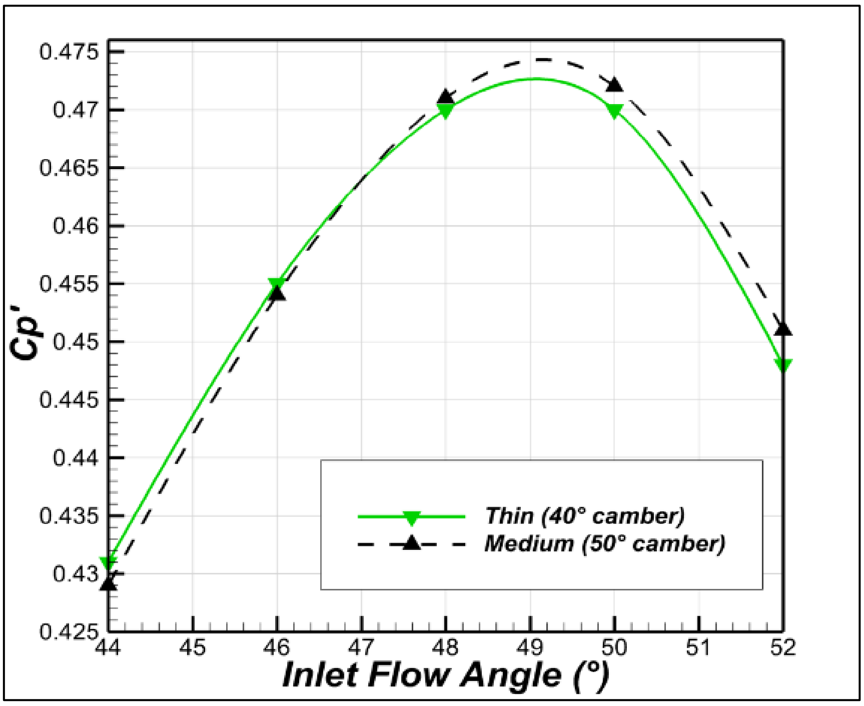

Figure 17: Static pressure rise coefficient versus inlet flow angle for thin and medium micro blades with 40° and 50° camber angle, respectively.
Source: Authors, (2026).

## III.4 STAGGER ANGLE EFFECTS

Following the analysis of thickness and camber effects, attention is now directed to the stagger angle. This parameter plays a critical role in governing flow turning and pressure rise characteristics. Figure 18 illustrates, for different inlet flow angles (β = 46°, 48°, 50°, 52°), how the Cp' and TPL vary with the MB stagger angle. for most of the tested β, Cp′ attains a maximum in the mid-stagger range (40° to 45°); at the same time, TPL exhibits a broad minimum in a similar stagger angle range. Beyond this band, the performance parameters deteriorate markedly, especially at β = 52°. The mid-stagger positions appear to best align the MB with the local flow, enhancing useful pressure rise while wake and mixing losses are minimized. A very large stagger produces boundary layer separation on the MB pressure side, causing adverse wake and blockage effects that increase TPL and reduce Cp'.

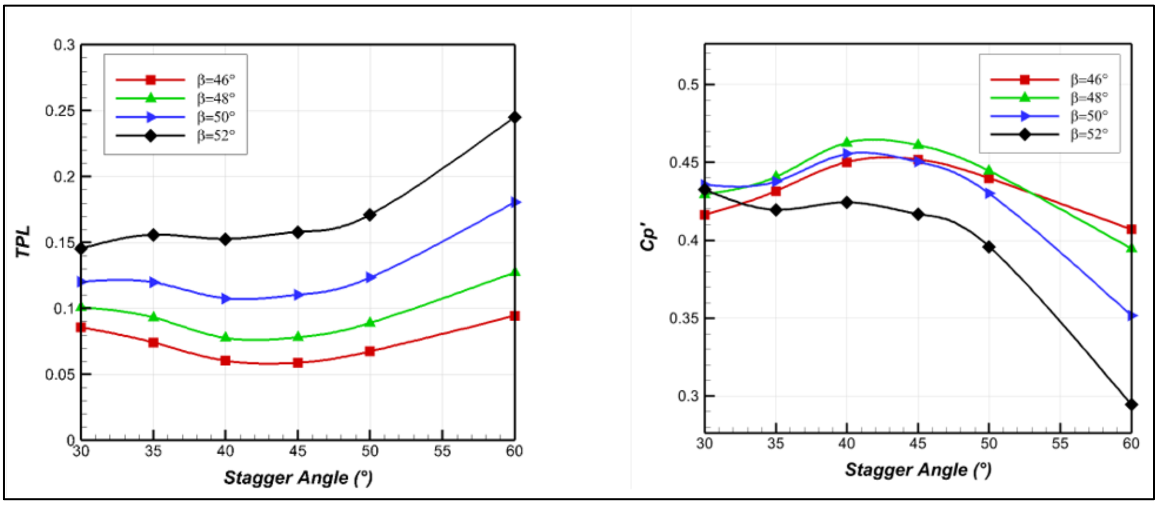

Figure 18: Variation of TPL (left) and Cp' (right) with MB's stagger angle for different β.
Source: Authors, (2026).

Using the selection criteria of maximizing static pressure rise Cp′, minimizing TPL, and preserving robustness across tested incidence angles, the mid-stagger band (40° to 45°) is the clear candidate. Between 40° and 45°, the plots show only small differences: 40° tends to produce slightly lower TPL and gives marginally higher Cp' across the majority of studied β. Therefore, as a conservative and robust choice, we select stagger = 40° as the preferred setting.

## III.5 CHORD LENGTH EFFECTS

The influence of MB chord length on cascade losses is examined by comparing the TPL across different inlet flow angles. As shown in Figure 19, the chord is expressed as a percentage of the main blade chord. For all studied incidences, TPL decreases with increasing MB chord up to an intermediate size, where the TPL attains its minimum value observed in the range of 20% to 25% of the main blade chord, with the 20% case providing the lowest TPL across all incidence angles except for □ = 52°.

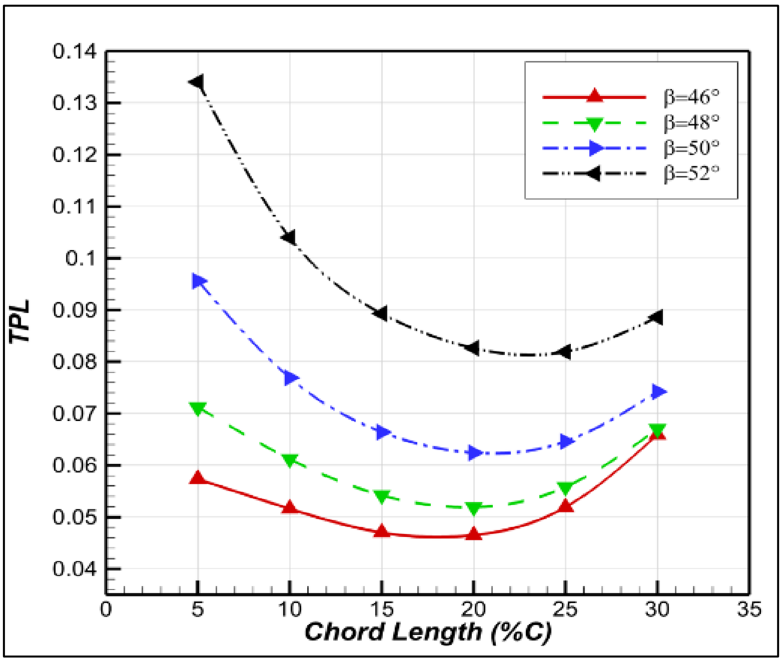

Figure 19: TPL versus micro-blade chord length with different off-design β.
Source: Authors, (2026).

To better understand these trends, it is necessary to consider the balance between the interaction area, boundary layer energization, and blockage related to the MB size effects. At low chord lengths (5%*c* to 10%*c*), the MB offers a limited interaction area, which proves insufficient boundary layer-MB interactions resulting in relatively high TPL values. Increasing the chord to intermediate values (15%*c* to 25%*c*) enhances the exchange of momentum between the freestream and near-wall flow, which contributes to the boundary layer energization without providing excessive blockage and wake losses. This compromise explains the observed minimum in TPL. Beyond this optimum range, larger chords (>25%) act as geometric obstacles, intensifying the local pressure gradients, the associated blockage and wake thickening outweigh the benefits of momentum exchange, leading to TPL rise. The evaluation of the velocity contour distributions with and without MB provides further insight into the mechanisms by which the MB enhances aerodynamic performance. As illustrated in Figure 21, it is evident that the suction side boundary layer for the baseline case experiences progressive thickening with increasing inflow angle (see Figure 20), ultimately leading to extended flow separation and the development of large low momentum regions. This effect is particularly pronounced for β = 50° and β = 52°, where massive separation occupies a significant portion of the suction surface, and the downstream wake region exhibits a large momentum deficit.

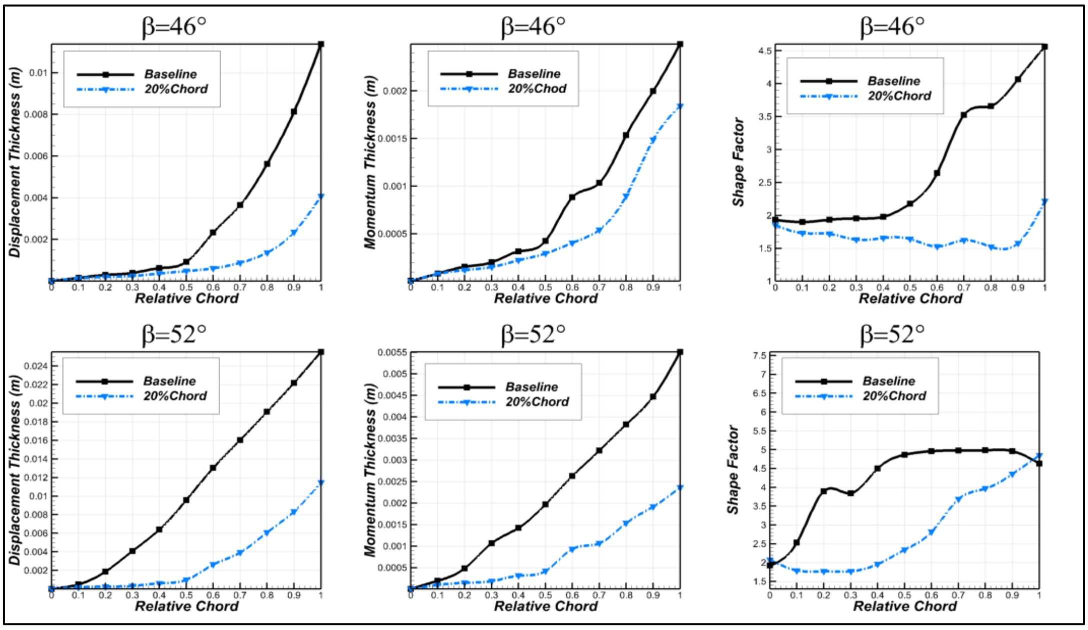

Figure 20**:** Displacement thickness, momentum thickness, and shape factor for Baseline and optimal flow control configuration: top β = 46°, bottom β = 52°.
Source: Authors, (2026).

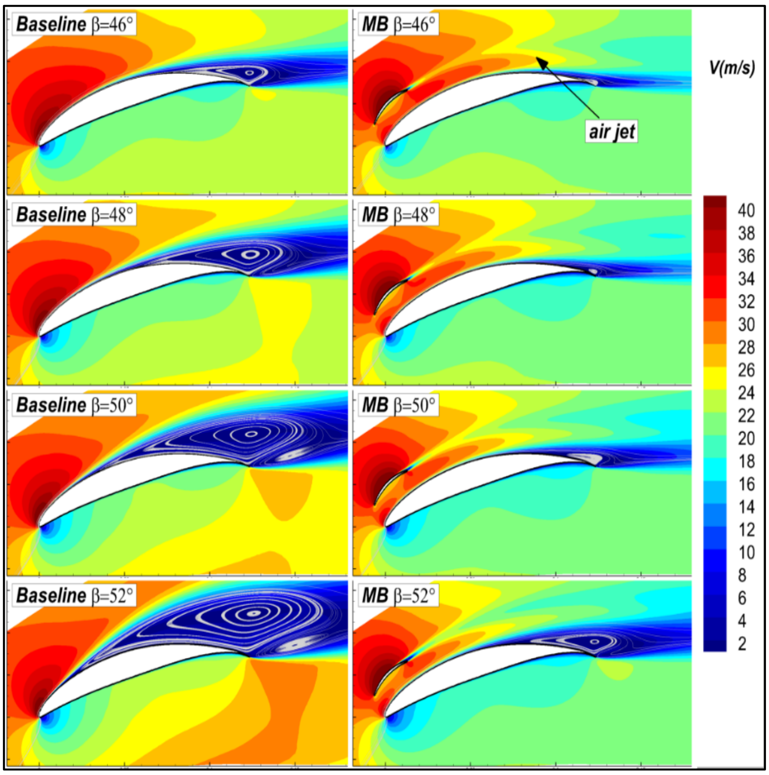

Figure 21**:** Velocity contours for the baseline (left) and controlled (right) cases at different inlet flow angles**.**
Source: Authors, (2026).

The controlled cases with the MB reveal a substantially modified flow field; the acceleration region near the main blade leading edge separates into two parts, allowing the high momentum fluid to develop and entrain into the boundary layer, building an air jet barrier preventing the boundary layer growth and separation [12]. The beneficial effect of this mechanism is manifested in the delayed separation onset. At high inlet flow angles (50° and 52°), where the baseline configurations exhibit massive separation, the MB cases maintain attached flow over a much longer chord extent, with thinner wakes and reduced low velocity regions downstream.

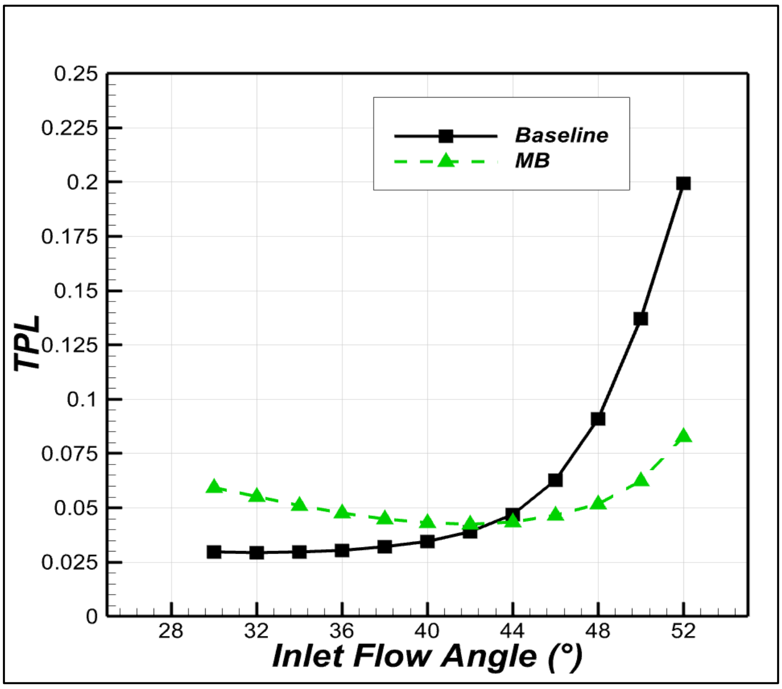

Figure 22**:** TPL for the baseline and optimal MB under design and off-design inlet flow angles**.**
Source: Authors, (2026).

Figure 22 compares the TPL variation with inlet flow angles from 30° to 52° for both baseline and optimal MB configurations. At low inlet angles (below 44°), both configurations exhibit relatively small loss coefficients, indicating attached and stable flow conditions. However, the MB case shows slightly higher TPL values in this range. This penalty is attributed to additional losses generated near the micro-blade pressure side, where its boundary layer is largely separated due to the relatively high stagger angle. As the incidence increases beyond 44°, the performance difference between the two configurations becomes beneficial. While the baseline configuration experiences a sharp rise in TPL, indicating stall onset, the MB configuration maintains much lower losses. This behavior demonstrates the device's strong capability to delay separation and stabilize the flow under near-stall conditions. Notably, the largest improvement is observed at the stall condition when β=52°, the optimized micro-blade achieves a 55.56% reduction in TPL compared to the baseline. This confirms that the optimized geometry and placement effectively mitigate boundary layer separation at critical operating points. Overall, the trend highlights the incidence sensitivity of the device; while it may introduce penalties at nominal conditions, it provides aerodynamic benefits under off-design regimes, thereby extending the compressor's stable operating range.

## III.6 OPTIMAL MB EFFECTS ON 3D FLOW STRUCTURES

Figure 23 compares the pitchwise mass-averaged TPL distribution across the half-span at a plane located 1.5 chords downstream of the main blade leading edge at different inlet flow angles. At the nominal design angle (□ = 32°), the configuration produces a slight increase in losses. This behavior is consistent with the optimization basis; the MB geometry was designed to counteract flow degradation occurring under off-design conditions, where the effects of separation and secondary flows are more significant.

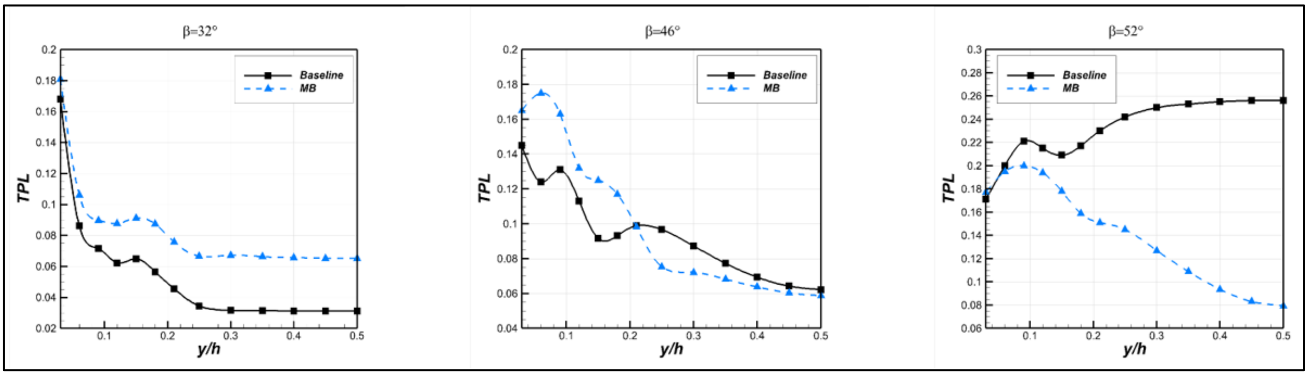

Figure 23: Pitchwise mass-averaged TPL across half-span of the MB and baseline cases for different $\beta$.
Source: Authors, (2026).

The observed behavior confirms that the device's effectiveness is very sensitive to the inlet flow angle. Figure 24 shows the TPL contours at the measurement plan. The MB configuration at nominal inlet flow angle produces a broader wake region and slightly higher overall losses compared with the baseline (BSL) case. The relatively high stagger and camber angles promote a pressure side boundary layer separation that forms on the MB itself, generating a large wake extent. Nevertheless, the losses near the endwall suction side corner remain marginally greater than those obtained of the baseline configuration, indicating that the control device does not significantly affect the corner separation at this operating point. At β = 46°, the TPL contours show that, once the MB is introduced, the region of highest loss becomes concentrated much closer to the endwall, while losses decrease above roughly 20% span (see Figure 23), the net benefit peaks toward mid-span, and the wake related to the MB is significantly reduced. The corresponding limiting streamlines and axial velocity iso-surfaces at the same incidence are shown in Figure 25; the suction-side topology directly supports the early observation; the MB case displays a more compact corner separation compared with the baseline, indicating that the MB reduces the corner separation spanwise extent. At β = 52°, the baseline case shows a very large separation (Figure 25); the MB case still exhibits a large separation region, but it appears more compact, and the surrounding streamlines show a different topology than the baseline. The relative improvement produced by the MB is largest at high incidences; the MB reduces the separated area most visibly under those conditions. At the highest incidence (52°), the MB still alters the topology but does not eliminate the dominant separation seen in the baseline.

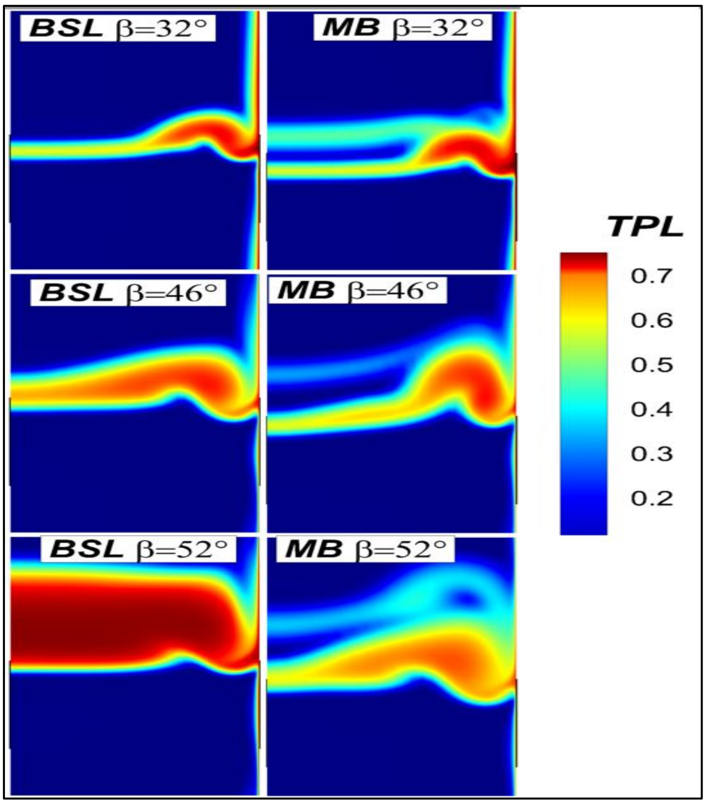

Figure 24**:** TPL contours at the measurement plane of MB and baseline cases under both nominal (up) and off-design (down) inlet flow angles.
Source: Authors, (2026).

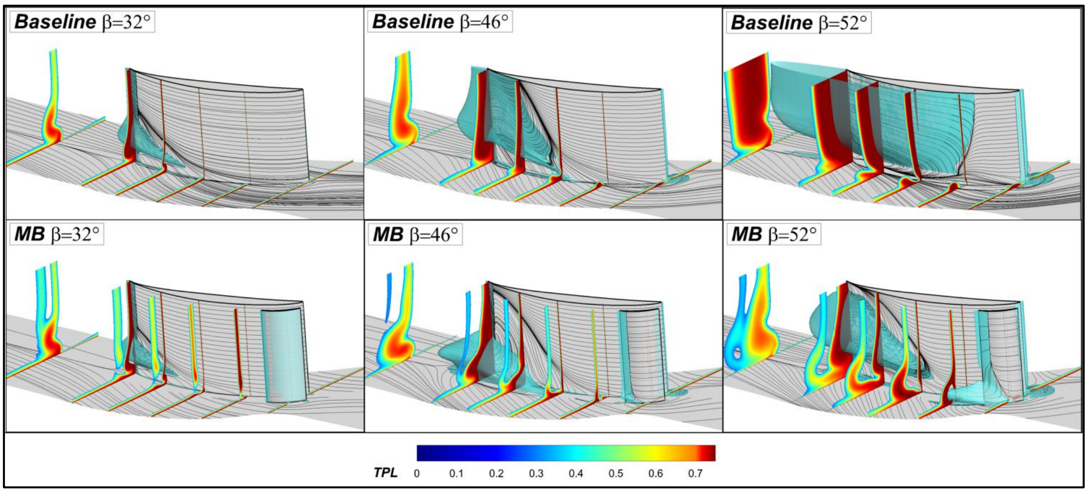

Figure 25**:** Limiting streamlines, TPL contours, and axial velocity iso-surfaces at -0.001 m/s of MB and baseline cases under different $\beta$.
Source: Authors, (2026).

## IV. CONCLUSIONS

This work combined an extensive two-dimensional parametric study with targeted three-dimensional calculations to evaluate micro-blade passive control in a NACA 65(18)10 linear compressor cascade. The influence of the MB's spatial positioning on the cascade performance is strongly affected by its axial position, whereas the circumferential location has a comparatively minor influence. The 2D optimization study on camber angle highlights a critical balance between boundary layer energization and wake losses. Local diagnostics show that the flat MB modifies the static pressure distribution near the main blade LE, causing a local acceleration, a fuller near-wall profile, and reduced momentum thickness compared with both the baseline and cambered MB. Crucially, Cases that appear favorable by locally thinning the boundary layer may still produce stronger wakes, ultimately raising the TPL. Small elements fail to provide sufficient momentum exchange, while large elements act as obstacles, causing strong wake losses. A micro-blade staggered at 40°, a chord length of 20%*c* with a medium maximum thickness (5%□□□) and 50° camber, has delivered the best balance between energizing the suction side boundary layer and avoiding excessive blockage

The controlled cases with the MB reveal a substantially modified flow field. The acceleration region near the main blade leading edge separates into two parts, allowing the development and entrainment of high momentum fluid into the main blade suction side boundary layer. The 3D cascade simulations reinforced the conclusions of the 2D analysis, revealing a penalty in losses at the nominal design incidence, and the beneficial effects of the device become pronounced at off-design incidences, indicating a strong sensitivity of the MB's performance to the inlet flow angle. Under off-design conditions, the MB weakens the corner separation and reduces its spanwise extent. The residual high losses are shifted to the endwall region. Future investigations should focus on a more detailed three-dimensional analysis to better capture the complex secondary flow interactions and endwall effects. In particular, determining the optimal spanwise distribution of the MB will be essential to fully exploit their potential for corner flow control and overall loss reduction.

## V. AUTHOR'S CONTRIBUTION

**Conceptualization:** Oussama Hachelfi.
**Methodology:** Oussama Hachelfi.
**Investigation:** Oussama Hachelfi.
**Discussion of results:** Oussama Hachelfi and Riyadh Belamadi.
**Writing – Original Draft:** Oussama Hachelfi.
**Writing – Review and Editing:** Oussama Hachelfi and Riyadh Belamadi.
**Resources:** Oussama Hachelfi.
**Supervision:** Riyadh Belamadi and Naouam Boudinar.
**Approval of the final text:** Oussama Hachelfi, Riyadh Belamadi, and Naouam Boudinar.

## VI. ACKNOWLEDGMENTS

This research is a result of the PRFU Project A11N01EP230220220001 funded in Algeria by La Direction Générale de la Recherche Scientifique et du Développement Technologique (DGRSDT).

## VII.REFERENCES

[1] M. EL-Sheikh, H. M. EL-Batsh, E.-S. Zanoun, and A. M. Attia, "Numerical and experimental investigations of flow separation control through a linear compressor cascade", Discover Applied Sciences, vol. 6, no. 9, pp. 450. Aug. 2024. doi: https://doi.org/10.1007/s42452-024-05982-3.

[2] O. Dumitrescu, E.-G. Prisăcariu, and V. Drăgan, "Review of Passive Flow Control Methods for Compressor Linear Cascades", Applied Sciences, vol. 15, no. 7, pp. 4040. Apr. 2025. doi: https://doi.org/10.3390/app15074040.

[3] R. Putzu, M. Carta, T. Ghisu, S. Shahpar, and A. Kovanis, "Secondary Flows Control in a Modern Aero-Engine Fan using Vortex Generators", Aerospace Science and Technology, vol. no. pp. 110468. Oct. 2025. doi: https://doi.org/10.1016/j.ast.2025.110468.

[4] S. Sun, L. Zhou, Y. Zhu, H. Zhu, T. Meng, and L. Ji, "PIV investigation on corner separation control in a compressor cascade based on a vortex generator", Journal of Visualization, vol. 27, no. 2, pp. 159-175. Feb. 2024. doi: https://doi.org/10.1007/s12650-024-00962-6.

[5] Y. Chen, L. Yang, and J. Zhong, "Numerical study on endwall fence with varying geometrical parameters in a highly-loaded compressor cascade", Aerospace Science and Technology, vol. 94, no. pp. 105390. Nov. 2019. doi: https://doi.org/10.1016/j.ast.2019.105390.

[6] A. Hergt, R. Meyer, and K. Engel, "Effects of vortex generator application on the performance of a compressor cascade", Journal of Turbomachinery, vol. 135, no. 2, pp. 021026. Mar. 2013. doi: https://doi.org/10.1115/1.4006605.

[7] A. Hergt, R. Meyer, and K. Engel. (Jan. 2006). Experimental investigation of flow control in compressor cascades, Turbo Expo: Power for Land, Sea, and Air, 4241, 231-240.doi https://doi.org/10.1115/GT2006-90415.

[8] A. M. Diaa, M. F. El-Dosoky, O. E. Abdel-Hafez, and M. A. Ahmed. (2014). Secondary flow control on axial flow compressor cascade using vortex generators, ASME International Mechanical Engineering Congress and Exposition, 46421, V001T01A069.doi https://doi.org/10.1115/IMECE2014-37790.

[9] J. Zhong, J.-A. Han, Y. Liu, and F. Tian. (2008). Numerical simulation of endwall fence on the secondary flow in compressor cascade, Turbo Expo: Power for Land, Sea, and Air, 43161, 509-518.doi https://doi.org/10.1115/GT2008-50888.

[10] M. Shan, C. Wuli, and L. Xiangjun, "A combined application of micro-vortex generator and boundary layer suction in a high-load compressor cascade", Chinese Journal of Aeronautics, vol. 32, no. 5, pp. 1171-1183. May 2019. doi: https://doi.org/10.1016/j.cja.2019.03.034.

[11] J.-L. Shen, H.-C. Yang, and S.-I. Yeh, "Fish Scale-Inspired Flow Control for Corner Vortex Suppression in Compressor Cascades", Biomimetics, vol. 10, no. 7, pp. 473. Jul. 2025. doi: https://doi.org/10.3390/biomimetics10070473.

[12] B. Wang, and Y. Wu, "Passive flow control of the corner separation in an annular compressor cascade with a micro-blade", Proceedings of the Institution of Mechanical Engineers, Part A: Journal of Power and Energy, vol. 233, no. 3, pp. 293-308. Jul. 2019. doi: https://doi.org/10.1177/0957650918787882.

[13] S. Ma, and X. Sun, "Optimization study on the influence of little blades' spatial position on a compressor cascade performance", Proceedings of the Institution of Mechanical Engineers, Part G: Journal of Aerospace Engineering, vol. 236, no. 9, pp. 1799-1816. Oct. 2022. doi: https://doi.org/10.1177/09544100211044327.

[14] Z. Guo, W. Chu, and X. Chen. (2020). Study on Optimization Design and Flow Control Mechanism of Little Blades in a Compressor Cascade, Turbo Expo: Power for Land, Sea, and Air, 84065, V02AT32A072.doi https://doi.org/10.1115/GT2020-16179.

[15] F. R. Menter, "Two-equation eddy-viscosity turbulence models for engineering applications", AIAA journal, vol. 32, no. 8, pp. 1598-1605. May 1994. doi: https://doi.org/10.2514/3.12149.

[16] L. J. Herrig, J. C. Emery, and J. R. Erwin, "Systematic two-dimensional cascade tests of NACA 65-series compressor blades at low speeds", vol. no. pp. Sept. 1957. doi,

[17] M. Ramzi, and G. AbdErrahmane, "Passive control via slotted blading in a compressor cascade at stall condition", Journal of Applied Fluid Mechanics, vol. 6, no. 4, pp. 571-580. Oct. 2013. doi: https://doi.org/10.36884/jafm.6.04.20670

[18] Y. Takahashi, H. Hamatake, Y. Katoh, M. Toda, and Y. Kashiwabara. (2005). Experimental and numerical investigations of endwall flow in a bowed compressor cascade, 41st AIAA/ASME/SAE/ASEE Joint Propulsion Conference & Exhibit, 3638.doi https://doi.org/10.2514/6.2005-3638.

[19] S. Bouterra, R. Belamadi, A. Djemili, and A. Ilinca, "Microcylinder and slot combination for flow separation control over a wind turbine airfoil", Wind Energy, vol. 28, no. 7, pp. e70035. Jun. 2025. doi: https://doi.org/10.3390/en17225597.